Materials Characterization 185 (2022) 111675

Contents lists available at ScienceDirect

Materials Characterization

journal homepage: www.elsevier.com/locate/matchar

Studying GPI zones in Al-Zn-Mg alloys by 4D-STEM

E. Thronsen [a,*], J. Frafjord [a], J. Friis [a,b], C.D. Marioara [b], S. Wenner [a,b], S.J. Andersen [b], R. Holmestad [a]

[a] Department of Physics, Norwegian University of Science and Technology (NTNU), N-7491 Trondheim, Norway
[b] SINTEF Industry, N-7465 Trondheim, Norway

ARTICLE INFO

Keywords:
Aluminium alloys
Transmission electron microscopy (TEM)
Natural ageing
4D-STEM
Phase mapping
GP-zones

ABSTRACT

A new methodology has been developed to study the fine details of GP zones in age-hardenable aluminium alloys. It is complementary to atomic resolution high-angle annular dark-field scanning transmission electron microscopy imaging, and combines scanning precession electron diffraction with diffraction simulations. To evaluate the method, data was collected from an Al-Zn-Mg alloy in a condition with a dense distribution of GPI zones. Diffraction patterns were recorded in the ⟨001⟩Al orientation, capturing GPI zones in three projections: along the unique [001]GPI axis, and along the two other mutually orthogonal orientations. The GPI zones viewed along [001]GPI revealed how the truncated octahedron units of the GPI zones were connected in multi-unit GP zones, while the two orientations normal to [001]GPI highlight the internal structure. The stability of the atomic models developed based on the experimental results was verified by density functional theory calculations.

1. Introduction

Transmission electron microscopy (TEM) is a powerful and versatile tool for characterising materials on the nano scale. Its strength lies in its sub-nanometer resolution and the possibility of detecting multiple complementary signals simultaneously from the same region. With the advent of spherical aberration corrected TEMs, a more direct interpretation of atomic columns in an image is possible. This allows for studies of atomic details of extremely small particles and their interfaces with the host material. In this respect, atomically resolved high-angle annular dark field (HAADF)-scanning transmission electron microscopy (STEM) has proven very useful. The advantage of this technique is the incoherent nature of the image contrast, and an electron scattering power that increases monotonously with the atomic number of the imaged atomic column [1]. The advancement in the TEM field has had benefits for the understanding of hardening mechanisms in light alloys. For example, by combining *Z*-contrast atomic resolution HAADF-STEM and density functional theory (DFT) calculations, the crystal structure of key precipitates in a range of important age-hardenable Al alloys have been determined and verified [2,3].

The nano-sized precipitates are formed during what is normally the final processing step of age-hardenable aluminium alloys, known as artificial ageing (AA). The typical AA treatment in Al-Zn-Mg alloys is conducted at temperatures between 120°C and 200°C. The objective is to obtain a high number density of fine, semi-coherent precipitates which will optimize the dislocation pinning effect, maximising the hardness of the alloy. During ageing, the mobilities of solutes and vacancies are several factors higher than at room temperature (RT) and the hardness gradually increases as precipitates nucleate, grow and transform. The AA treatment is always preceded by the solution heat treatment (SHT) or other high-temperature processing, performed above the solvus line (typically 450°C for the Al-Zn-Mg system). Between SHT and AA, a fast cooling to RT is usually conducted, which creates a state of supersaturated solid solution (SSSS). In this state, most solutes are dissolved in the Al lattice, and the vacancy concentration may be several orders of magnitude higher than normal, depending on the quench rate. The state is unstable and if kept at RT, clusters form accompanied by a gradual increase in hardness [4,5]. This process is known as natural ageing (NA). When the clusters achieve periodic order in one or more spatial dimensions obtaining characteristic shapes (plates, spheres or needles) they are often referred to as Guinier-Preston (GP) zones after their discoverers in 1938 [6,7]. The clusters, GP zones and precipitates all influence the material properties. In the Al-Zn-Mg alloy system, two types of GP zones with different structure have been found to exist, namely the GPI- and GPII zones [8]. The current work contributes to expand the knowledge of the nature of the GPI zones.

Recently the crystal structure of the GPI zones forming during NA and the initial stage of AA were determined by a combination of HAADF-

* Corresponding author at: Department of Physics, Norwegian University of Science and Technology (NTNU), N-7491 Trondheim, Norway.
E-mail address: Elisabeth.thronsen@ntnu.no (E. Thronsen).

https://doi.org/10.1016/j.matchar.2021.111675
Received 14 September 2021; Received in revised form 23 November 2021; Accepted 9 December 2021
Available online 15 December 2021

STEM experiments/simulations and DFT calculations [9]. These GPI zones have been known and investigated for decades [8,10–13]. By taking advantage of the HAADF-STEM technique, the study showed that the GPI zones are built up by a single building block: Mg and Zn atoms order in the matrix on and around an fcc Al cell, forming a high symmetry shell-structure termed truncated cube octahedron (TCO). This is shown in Fig. 1a: The inner shell is an octahedron formed by the six faces centres, occupied by Zn atoms. The second shell is the eight Mg corners. The third shell is a TCO defined by 24 vertices, fcc positions immediately surrounding the cube, ideally occupied by Zn. In addition, the TCO may incorporate an interstitial site at the octahedral centre in the cell. This is emphasised by the dark centre atom in Fig. 1a. The unit was found to connect along three Al directions to form larger GPI zones: along ⟨001⟩, ⟨411⟩ and ⟨330⟩. The three different ways of connecting the TCOs are shown in Fig. 1b. The structure shows best contrast along its unique axis [001]GPI (left) where the TCOs share 4-fold faces, forming strings. The central column in a TCO string is special: It incorporates the main distinction from the fcc Al lattice as it can contain interstitials or vacancies. Along [001]GPI, the connection between two TCOs is denoted '[002]' to emphasise that the two tcos are separated by two Al-periods (8.1 Å). The lateral connections between TCOs in neighbour strings share edges (right hand side of Fig. 1b) and are termed '⟨411⟩' and '⟨330⟩'. Both measure 8.59 Å. The GPI zone with highest symmetry has TCO strings joined in ⟨411⟩ directions only, producing a 4-fold helix around [001]GPI. It has the tetragonal space group P41 (#76) [9] and will be termed '⟨411⟩ connected GPI zone'. Mixing of the lateral connection ⟨411⟩ and ⟨330⟩ in one zone is common, hence the individual GPI zones show variation in structure. These zones are referred to as '⟨330⟩-⟨411⟩ connected GPI zones'.

The HAADF-STEM approach is not always applicable for studying GP zones in age-hardenable Al alloys. The GP zones in Al-Zn-Mg and Al-Mg-Si alloy systems appear to be spherical with a diameter of 1-3 nm [14–17]. The regions investigated in electropolished TEM foils are typically up to 40 nm thick, implying a low GP zone/Al signal. In addition, zones overlap along the viewing direction. Alternative experimental techniques and complementary modelling are therefore needed. The Al-Zn-Mg alloy system has the advantage of exhibiting a strong *Z*-contrast due to the atomic numbers being 13, 30 and 12 respectively. This alloy system is therefore ideal for validating newly developed methods for studying GP zones in alloy systems where the Z-contrast is weaker.

With the new generations of cameras for TEM, direct electron detectors DED [18], together with a progress in computing power, 4D-STEM has gained recognition as a versatile and robust technique. In 4D-STEM, a convergent probe scans a 2D region of the specimen while recording the diffraction pattern for every probe position, creating a 4D dataset [19]. A subclass of 4D-STEM is scanning precession electron diffraction (SPED) [20]. For each real-space pixel, the beam is scanned at a constant angle, known as the precession angle, around the optical axis. The beam is de-scanned below the specimen. The net effect is equivalent to precession of the specimen around a stationary beam [21]. Recently, SPED was used to quantify the relative amount of different precipitate phases in Al alloys [22–24] and gave information about the crystallographic relationships of composite/intergrown precipitates [25]. The aim of the present work is to apply SPED to investigate the structure of the GPI zones and the role of the TCOs as fundamental building blocks in the GPI zones in the Al-Zn-Mg alloys. In combination with DFT calculations and diffraction pattern simulations, we explore a likely development path from the solid solution. One aim is to establish a general, robust methodology for studies of ordered clusters and GP zones in all age-hardenable Al alloys.

2. Material and methods

2.1. Material

A high purity lab-cast alloy with composition Al-3.49Zn-1.89 Mg (at. %) was used in this work. The alloy was prepared at University of Toyama. It was homogenized at 470°C for 24 h, extruded at 405°C and then cold-rolled into 0.3 mm thick sheets, being identical to what was used in a previous experiment [9]. The alloy underwent SHT at 475°C for 1 h before it was quenched in water and left at room temperature for 4 days. It was subsequently hardened by AA for 8 min at 120°C.

TEM specimens were prepared by mechanical grinding to ~60 μm thickness, from which 3 mm diameter discs were punched. The disks were electropolished with a Struers TenuPol-5 machine using an electrolyte mixture of 1/3 HNO_3 and 2/3 CH_3OH. The liquid was kept at −25°C±5°C and the applied voltage was 20 V.

2.2. Transmission electron microscopy

2.2.1. HAADF-STEM

An image- and probe corrected JEOL ARM200CF microscope operated at 200 kV was used to acquire the HAADF-STEM images and the selected area electron diffraction patterns (SADP). For the STEM acquisition, the convergence semi-angle was 27 mrad and the inner and outer collection semi-angles were 67 mrad and 155 mrad, respectively. The probe current was about 60 pA, which gives a good signal and sufficient spatial resolution. The HAADF-STEM images were filtered by performing a fast Fourier transform (FFT) and then applying a low-pass mask on the FFT of approximately 6.7 nm^{-1} before performing an inverse FFT.

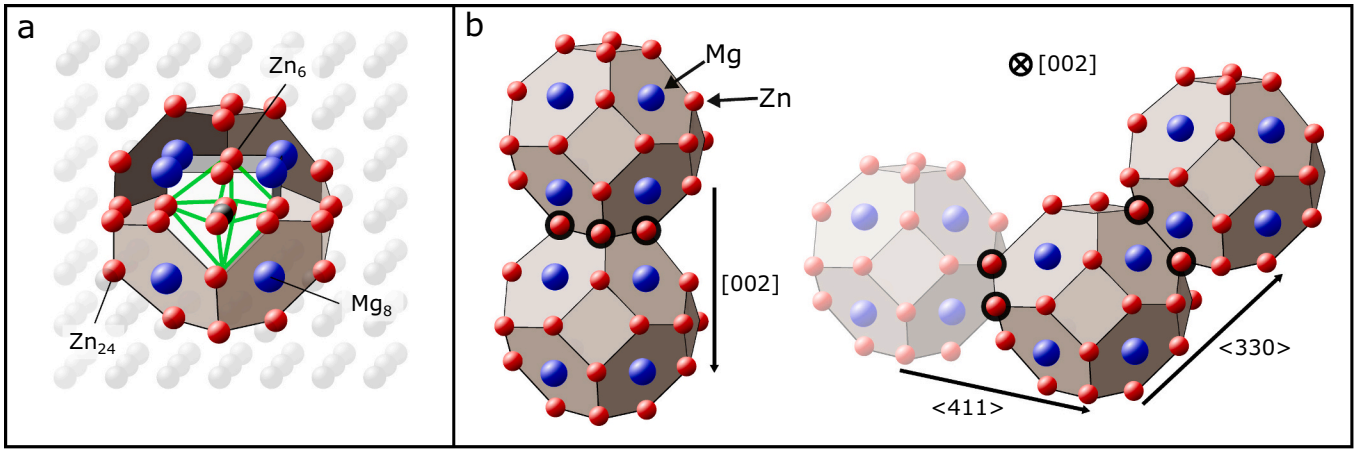

Fig. 1. a: Basic TCO molecular unit of the GPI zones. b: TCO connections in GPI zones. Left: two TCOs connected along [002] forming a TCO string. Right: Lateral sharing of TCO strings in ⟨411⟩ and ⟨330⟩ directions viewed along [001]GPI. Figure adapted from Ref. [9]. The black perimeter indicates shared atoms.

2.2.2. SPED acquisition and data analysis

A JEOL 2100F microscope operated at 200 kV was used in the experiments. The microscope was operated in nanobeam diffraction (NBD) mode, with a convergence angle of 1 mrad. The precession-angle and frequency was 0.3° (=5.2 mrad) and 100 Hz, respectively. The probe size was set to 0.5 nm, which is the smallest probe size available in the NBD mode with this instrument. Due to precession and aberrations, the actual probe size is larger, around 1–2 nm. The double-rocking probe was aligned according to the approach described by Barnard et al. [26] using the NanoMEGAS DigiSTAR control software. The SPED was performed using the NanoMEGAS P1000 scanner scan generator. The scan step size was set to 0.3 nm, and the scan regions were in the range of 100 × 100 - 300 × 300 pixels^2 corresponding to 30 × 30 - 100 × 100 nm^2. The 4D SPED datasets were recorded using a Medipix3 MerlinEM camera with a single 256 × 256 Si chip from Quantum detectors [27]. Diffraction patterns were recorded in 12 bit mode with an exposure time of 30–60 ms per pixel.

The SPED data was analysed using the open-source python libraries *hyperspy* [28] and *pyxem* [29]. The workflow is illustrated in Fig. 2. First, the 4D data matrix was acquired as described above. To inspect the data, virtual imaging was performed. By integrating the intensity of the diffraction patterns within a virtual aperture set in reciprocal space, a virtual dark-field (VDF) image was created. Binary masks were created both in the real- and reciprocal space using the python library *scikit-image* [30]. For the reciprocal-space mask, a blob-finding algorithm was used to locate the Al reflections in the average PED pattern of the entire data stack and subsequently masking out those reflections. The real-space mask was created in the following way: first the uneven background in the VDF image was accounted for using a rolling ball correction [31]. Next, the remaining background was subtracted by filtering regional maxima before a white tophat procedure was applied on the output image [32]. Finally, the binary VDF was created using a suitable intensity threshold. Each connected region in the binary VDF was assigned to an individual GP zone, and the PED patterns belonging to each zone was averaged to minimize the pattern noise. The result is a simplified dataset, with unchanged Al matrix, but with each zone assigned to its average PED pattern. The unsupervised learning routine, non-negative matrix factorisation (NMF) [33], was performed on the original datasets to check the validity of the simplified datasets. During the NMF decomposition, the Al reflections were masked out using the reciprocal space mask. The NMF routine decomposes the dataset into component maps, resembling diffraction patterns, and loading maps, resembling VDF images, showing where each particular component is important. By trial-and-error, a total of 5–10 components were deemed sufficient for each dataset. For etailed descriptions of NMF of SPED data confer Ref. [34]. An example of phase mapping can be found in Ref. [23].

To enhance the contrast between the diffraction spots and the background, which also makes the intensity distribution of the experimental patterns comparable to their simulated representations, the following pixel-by-pixel transformation was applied to the average PED patterns:

$$I_{\text{enhanced}} = 1 - e^{-I_{\text{initial}}/n}, \tag{1}$$

where I_{enhanced}, I_{initial} are the intensities in the enhanced and original image, respectively, while n is set to the typical maximum intensity in a GP zone diffraction spot. A value of 30 was used here.

2.3. Density functional theory

The DFT calculations were performed using the Vienna Ab Initio Simulation Package (VASP) [35,36], with the projector augmented wave method [37,38]. The generalised gradient approximation by Perdew-Burke-Erzenhof was the applied functional. The energy cutoff was set to 400 eV for all calculations.

The atomic model of the ⟨411⟩-connected GPI zone is illustrated in Fig. 3. The cell spans 6x6x2 Al unit cells. The double period of the supercell compared to the fcc along the [001] direction allows the central column of the TCO to be 3/2 occupied as compared to fcc Al. The system was first relaxed in a fixed volume with a gamma sampling of 0.18 Å^{-1}, afterwards, a maximum distance of k-points was set to 0.08 Å^{-1} for the energy calculations. A higher k-point density was required for the smearing method.

The formation enthalpy was calculated by

$$\Delta H = E - \sum_X N_X E_X, \tag{2}$$

where E is the total energy of the simulation cell comprising the GP zone. The summation gives the energy contribution of the different elements

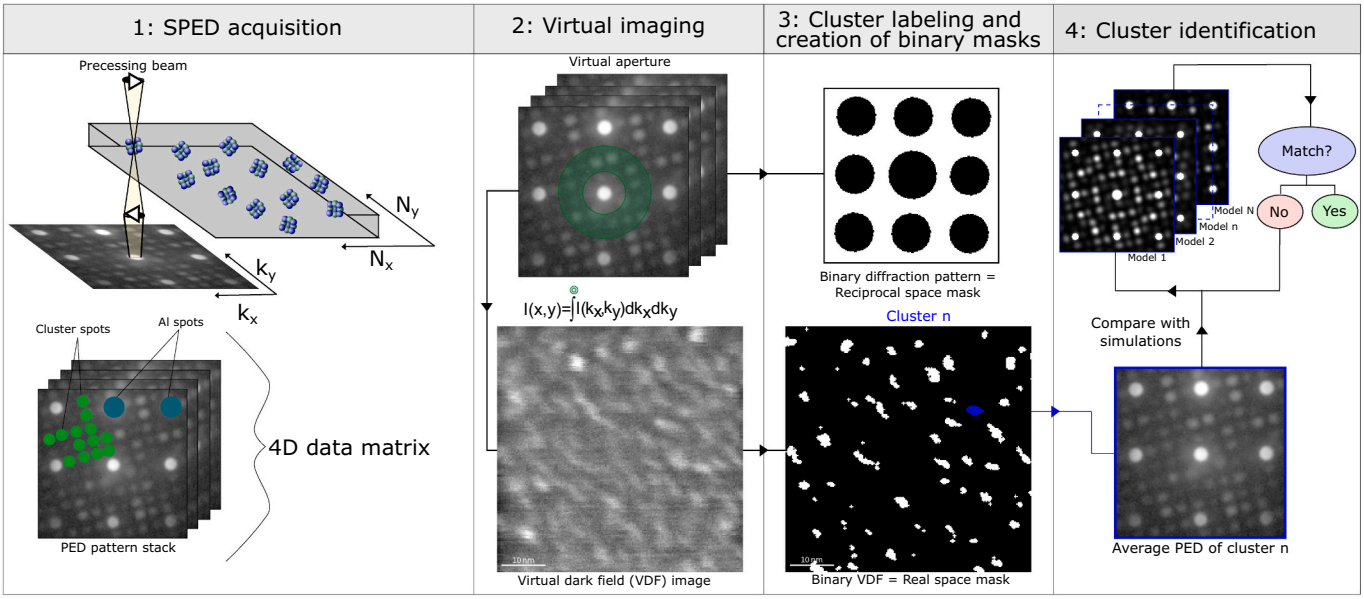

Fig. 2. Workflow of SPED experiments and data analysis showing the acquisition, the principle of virtual imaging, GP zone labelling, creation of binary masks and GP zone identification.

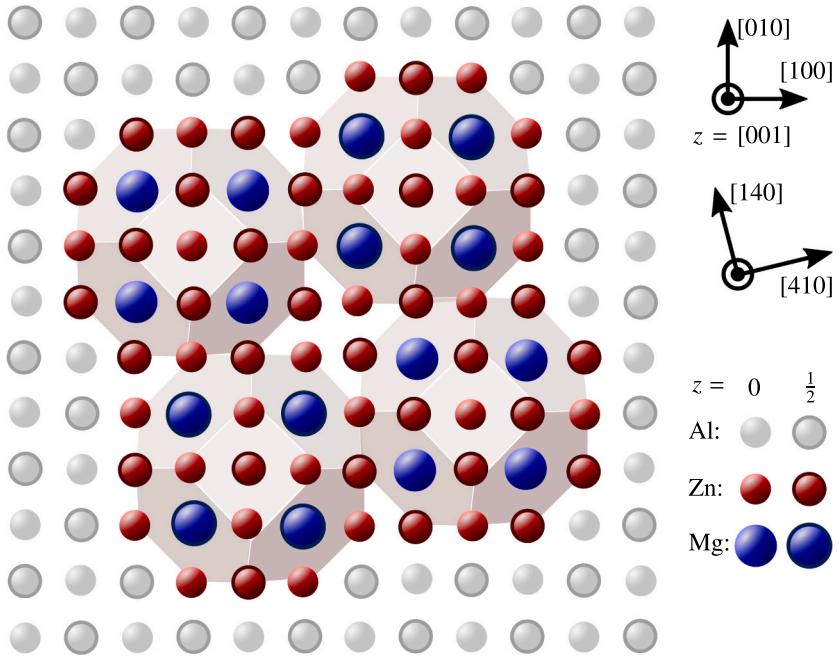

Fig. 3. Atomic model comprising a ⟨411⟩-connected GPI zone elongated in the [001] direction. The supercell spans 6x6x2 Al unit cells.

as single solutes in the matrix. N_X is the number of solutes of type X. E_X is the cohesive energy of element X in the aluminium matrix, per atom, and is calculated from a bulk configuration. The energy cost of the vacancies produced were also considered, as will be elaborated in the discussion section.

2.4. Diffraction pattern simulations

The multislice software μSTEM [39] was used to simulate the diffraction patterns in the position-averaged convergent beam electron diffraction (PACBED) mode. By setting the probe forming aperture to 1 mrad, mimicking the experimental condition, the resulting pattern will be an NBD pattern. Calculations were performed on a 512 × 512 pixels mesh grid. To obtain satisfactory resolution and simultaneously avoid wrap-around errors, a large supercell with dimensions 129 × 129 Å^2 was used, with layers of 13 Al unit cells surrounding the GPI zone model on each lateral side. The simulations were performed for thicknesses between 4 Å and 400 Å. Unless otherwise stated, the simulated diffraction patterns presented in the article are from a thickness of 48 Å.

To simulate PED patterns, a beam tilt of 5.2 mrad (= 0.3°) was introduced while rocking the tilted beam around the optical axis with increments of 4 mrad, resulting in a total of 1572 azimuthal angles. The final pattern represents an average of all the patterns. This is more computationally expensive than simulating NBD patterns. Hence, all the patterns presented in the article are NBD patterns, while PED patterns were simulated to investigate the effect of the precession compared to unprecessed patterns and are included in the Supplementary.

3. Results and discussion

3.1. Microstructure overview

The HAADF-STEM image in Fig. 4a shows the microstructure of the alloy in the ⟨001⟩Al projection. The dense population of GP zones comprises both ⟨411⟩- and ⟨330⟩-⟨411⟩ connected GPI zones. Note how all the atomically resolved zones are viewed along the unique [001]GPI axis. Fig. 4b shows a selected area diffraction pattern (SADP) from a region and orientation similar to Fig. 4a. The diffuse spots associated with the GPI zones are marked with yellow and green disks. Fig. 4c shows the FFT of Fig. 4a, exhibiting a good correspondence with the

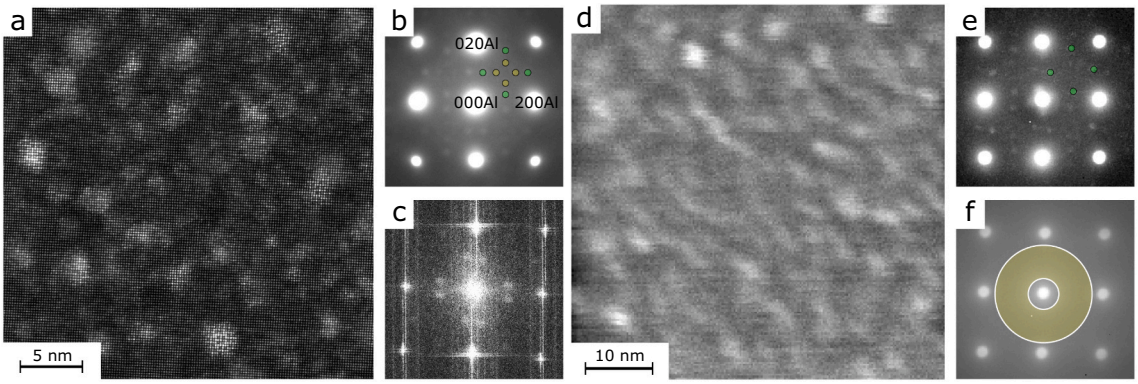

Fig. 4. a: HAADF-STEM showing a high density of GPI zones. b: SADP of a similar region as in a. c: fast Fourier transform of a. d: VDF image from a similar region as in a. e: Constructed pattern by maximum pixel values in the data stack. f: Average PED pattern illustrating the placement of the virtual aperture in the SPED data stack.

SADP in Fig. 4b. A VDF image from a 60 × 60 nm^2 region from one of the SPED datasets is shown in Fig. 4d. Fig. 4e is a constructed diffraction pattern with each pixel corresponding to its highest value in the 4D dataset. Fig. 4 f shows the average PED pattern from the same dataset, the overlay representing the virtual aperture. A bright pixel in the VDF image corresponds to a higher intensity within the virtual aperture in the corresponding PED pattern as compared to the rest of the diffraction patterns. Thus, higher intensity corresponds to solute ordering with longer periodicities than the basic Al period. The contrast in the VDF image appears stretched out because of stage drift during the acquisition.

The bright dots in the VDF image in Fig. 4d therefore indicate the presence of GPI zones or precipitates. Interestingly, there are no diffraction effects apart from the Al spots in the average PED patterns like Fig. 4f, while clear contributions from the GPI zones exist in the SADP, FFT and in the maximum patterns in Fig. 4b-c and e, respectively. This is understandable because the zones are small: The diameter of 1–3 nm [9] is small compared to the specimen thickness, which is the reason the GPI zone-to-Al signal is low. In the individual PED patterns, the intensity of the central disk is saturated, i.e. exceeding 4096 counts per detector pixel, while the Al diffracted disks have a typical count of 100–700. The GPI diffracted disks however, amount to 15–30 counts. In the PED patterns in the flat regions of the VDF image, the intensity between the Al diffracted spots is typically 6–15. The signal from the GPI zones is hence subdued by the background level in the average PED pattern in Fig. 4f.

3.2. Identification of unique PED patterns from GPI zones

Five PED patterns with unique diffraction effects were identified in the 4D data stack. To try to assess what type of structures gave rise to these PED patterns, NBD pattern simulations were performed based on different GPI models. The models are shown along [001]GPI, in column 1 in Fig. 5a-d. As mentioned, our previous work on the atomic structure of the GPI-zones indicated the presence of an interstitial position in the central column of the TCO strings [9]. Based on this, three models corresponding to four TCOs connected along the ⟨411⟩Al direction were set up. The difference between the models lies in the central column of the TCO: In the first model the solutes occupy the Al fcc lattice positions, hereby denoted 'fcc variant' and is shown in column 1 in Fig. 5a. Column 1 in Fig. 5b shows the 'defect variant', where the atoms of the central TCO column in a TCO string are displaced to the Al cell centres, i.e. the octahedral sites. This is a 1D column defect in the Al lattice, first identified in the β'' phase in the 6xxx system [40]. In the last ⟨411⟩ connected GPI zone model, the central column has 3/2 occupancy relative to Al, i.e. a fcc variant with every second octahedral site occupied. As opposed to the first two variants, the central columns have a period of 8.1 Å instead of 4.05 Å. This model is shown in column 1 in Fig. 5c and will in the following be denoted 'interstitial variant'. The extra solute in this configuration is delivered by the matrix, in exchange such columns can

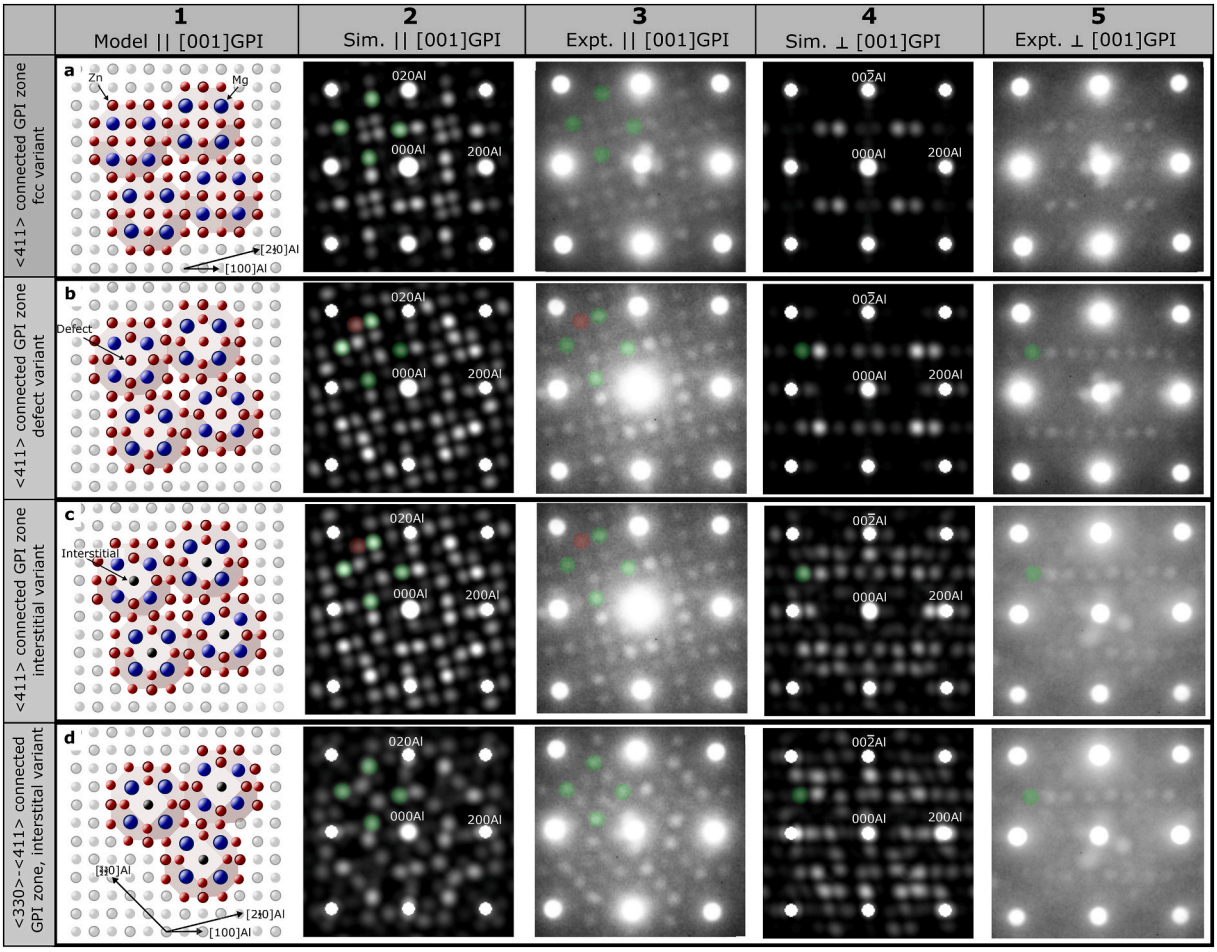

Fig. 5. GPI zone models and corresponding simulated NBD- and experimental PED patterns viewed parallel and normal to [001]GPI. Columns: (1) models along [001]GPI. (2,3) corresponding simulated patterns and selected experimental patterns, (4,5) simulated patterns and selected experimental patterns in one of the ⟨001⟩Al zone axes normal to [001]GPI. Rows: (a-c) ⟨411⟩ connected GPI zones with all solutes on fcc, with defected central column or with 3/2 occupancy in central columns, respectively, (d) ⟨330⟩-⟨411⟩ connected GPI zone with 3/2 occupancy in central columns. Note that all the simulations are NBD patterns, while the experimental patterns are PED patterns.

produce a vacancy every 8.1 Å. This is different from the defect variant, where the atoms of the central column are pushed into the octahedral site. In order to avoid too close spacing (2.025 Å) at the top and bottom of the GPI zone interfaces, a vacancy is locked, and by translation effectively split between the front and the end of the GPI zone.

The simulated NBD patterns corresponding to the three ⟨411⟩ connected variants along [001]GPI are shown in Fig. 5a-c, column 2. The reflections overlaid by green disks in the upper-left quadrant are of the same origin as the GPI reflections in the SADP in Fig. 4b. All three patterns inherit a 4-fold rotational axis. Visual comparison of selected diffraction spots shows that discrimination between the fcc variant and the two others is possible. For example, the reflections associated with the red disks in the patterns corresponding to the defect- and interstitial variants are absent for the fcc variant, indicating that such intensities are consequences of the interstitial ordering. The defect- and interstitial variants however, show strong similarity. Consequently, the diffraction patterns for these variants are indistinguishable in this projection. The experimental PED patterns in column 3 in Fig. 5a-c have a good correspondence with the simulated average NBD patterns. Note that in the experimental patterns, the reflections indicated by the red circles are faint, making it experimentally challenging to discriminate between the three variants in this orientation.

In addition to connecting purely along the ⟨411⟩Al directions, the TCO strings can also connect along the ⟨330⟩Al directions [9]. However, this was only observed by HAADF-STEM if the GPI zones also contained ⟨411⟩ connections. GPI zones structured this way will in the following be denoted ⟨330⟩-⟨411⟩ connected GPI zones. An example is shown in column 1 in Fig. 5d. The central column has 3/2 occupancy relative to Al, making this the interstitial variant of the ⟨330⟩-⟨411⟩ connected GPI zones. The corresponding simulated average NBD pattern is shown in column 2. The approximate 3-fold rotational symmetry of the inner reflections in the pattern makes it distinguishable from the 4-fold rotational symmetric patterns originating from the ⟨411⟩-connected GPI zones (cf. column 2 in Fig. 5a-c). The experimental PED pattern in column 3 in Fig. 5d has a good correspondence with the corresponding simulated pattern. Conclusively, the PED patterns from ⟨330⟩-⟨411⟩- and ⟨411⟩ connected GPI zones are distinguishable when viewed along [001]GPI. It is however more challenging to conclude whether the central column contains defects or interstitials.

Considering the tetragonal crystal structure of the GPI zones, NBD pattern simulations were also carried out along the directions normal to [001]GPI. The results are shown in column 4 in Fig. 5a-c for the ⟨411⟩-connected GPI zones. Column 5 in Fig. 5a-c shows experimental patterns with a strong resemblance with the simulated patterns in column 4. Thus, based on one 4D dataset only it is possible to extract information both along [001]GPI, showing how the TCO strings are connected, in addition to investigate the existence of point defects along the central column of the TCO. This is an important result, as proving the latter is challenging based on HAADF-STEM imaging alone since all the atomically resolved GPI zones imaged in the ⟨001⟩Al orientation are viewed along [001]GPI. The diffracted reflections originating from the GPI zones imaged along the direction normal to [001]GPI also contribute to the SADP in Fig. 4b, as illustrated by the green disks in column 5 in Fig. 5b-d. NBD simulations of the interstitial variant of the ⟨330⟩-⟨411⟩ connected GPI zones along the directions normal to [001]GPI were also carried out. The results are shown in column 4 of Fig. 5d. By comparing this pattern with the one in column 4 in Fig. 5c, it is concluded that the two different stackings of the TCO strings to form larger GPI zones are not possible to differentiate in reciprocal space in this orientation. The same experimental PED pattern as in column 5 in Fig. 5c is shown in Fig. 5d to illustrate the correspondence of this particular experimental pattern with both the simulations in column 4 in Fig. 5c-d. However, the two connections are distinguishable when the GPI zones are viewed along [001]GPI.

Similar NBD pattern simulations were also carried out for the ⟨330⟩-⟨411⟩ connected GPI zones with solutes on fcc and with defect. They are shown in Fig. 1 in the Supplementary. Similarly as for the ⟨411⟩ connected GPI zones, the simulated NBD patterns for the fcc variant are distinguishable from the defect- and interstitial variants, while the defect and interstitial variants are indistinguishable when viewed along [001]GPI. No experimental patterns could be identified as the fcc variant along [001]GPI. Along the directions normal to [001]GPI, the patterns are distinguishable and show some resemblance to the patterns from the corresponding ⟨411⟩ connected GPI variants. The differences are however less prominent than for the ⟨411⟩ connected GPI zones. Differentiating between the ⟨411⟩- and ⟨330⟩-⟨411⟩ connected GPI zones was not possible when the GPI zones were imaged normal to [001]GPI.

3.3. Investigating GP zones by SPED

The experimental PED patterns in Fig. 5 contain reflections with satisfactory correspondence with the simulated patterns of the different GPI zone models. In a 30 nm × 30 nm scan, typically 20 average PED patterns could be identified as originating from GPI zones. As mentioned above, viewing the GPI zones along [001]GPI allowed for separation between the ⟨411⟩- and ⟨330⟩-⟨411⟩ connected GPI zones, while viewing them along a direction normal to [001]GPI separated the fcc-, defect- and interstitial variants, amounting to a total of five categories. About 1/3 of the GPI zone diffraction patterns in any given scan could be matched with patterns of these five categories. The remaining GPI zone patterns could not be determined. The origin of such patterns is most likely overlapping GPI zones along the viewing direction, causing the corresponding PED pattern to be similar to the SADP in Fig. 4b. Overlap can be reduced by using a thin region of the TEM specimen. In our experience, a sample thickness of 20–40 nm is ideal. In thinner regions, the signal from the amorphous surface oxide layer tends to dominate.

In this work, a total of 39 patterns from 8 datasets were investigated and labelled manually to get an idea of the relative numbers of ⟨411⟩ connected GPI zones compared to ⟨330⟩-⟨411⟩ connected GPI zones. Fig. 6 shows one example, with the VDF image and the corresponding binary VDF image in Fig. 6a-b, respectively. Fig. 6c1-c4 show average PED patterns extracted from the region in the binary VDF image with the corresponding colour. The pattern indicated with turquoise (Fig. 6c1) corresponds to the ⟨411⟩ connected GPI zones. The patterns marked by yellow (Fig. 6c2) and orange (Fig. 6c3) correspond to GPI zones viewed normal to [001]GPI, with intensities corresponding the fcc- and defect variant, respectively. The pattern associated with purple is similar to the SADP in Fig. 4b. In Fig. 6d1-g1 and Fig. 6d2-g2, the results from an NMF analysis of the dataset are presented. The top row (Fig. 6d1-g1) shows component maps, while the bottom row (Fig. 6d2-g2) shows loading maps. The composite component- and loading maps in Fig. 6d1-d2 are the sum of all components associated with GPI zones. The individual NMF components are shown in Fig. 6e1-g1 and Fig. 6e2-g2, using the same colour scheme as in Fig. 6c1-c3. By comparing the simplified dataset from the binary VDF image with the results from the NMF decomposition, it was observed that the loading maps of specific components from the NMF corresponded well to the simplified dataset. It is interesting to note that the set of inner reflections marked by yellow disks in Fig. 4b stem from the GPI zones viewed normal to [001]GPI, as evidenced in the composite component map in Fig. 6d1. The average PED pattern in Fig. 6c4 has more resemblance with the SADP in Fig. 4b than with any of the simulated patterns along [001]GPI. This indicated that this particular pattern is a mix of GPI zones in the three orientations, most probably due to overlap of multiple zones along the viewing direction. This complicates the analysis as the NMF categorises the overlapped GPI zones as ⟨411⟩ connected GPI zones, evidenced in Fig. 6e2. Thus, the NMF succeeds at separating the GPI zones viewed normal to [001]GPI, but fails at separating the ones viewed along [001]GPI if overlapping GPI zones are present. Care should therefore be taken if using NMF to extract information about the relative amounts of GPI zones along [001]GPI. In the following, results from the manual labelling of patterns from the binary VDF image will be discussed.

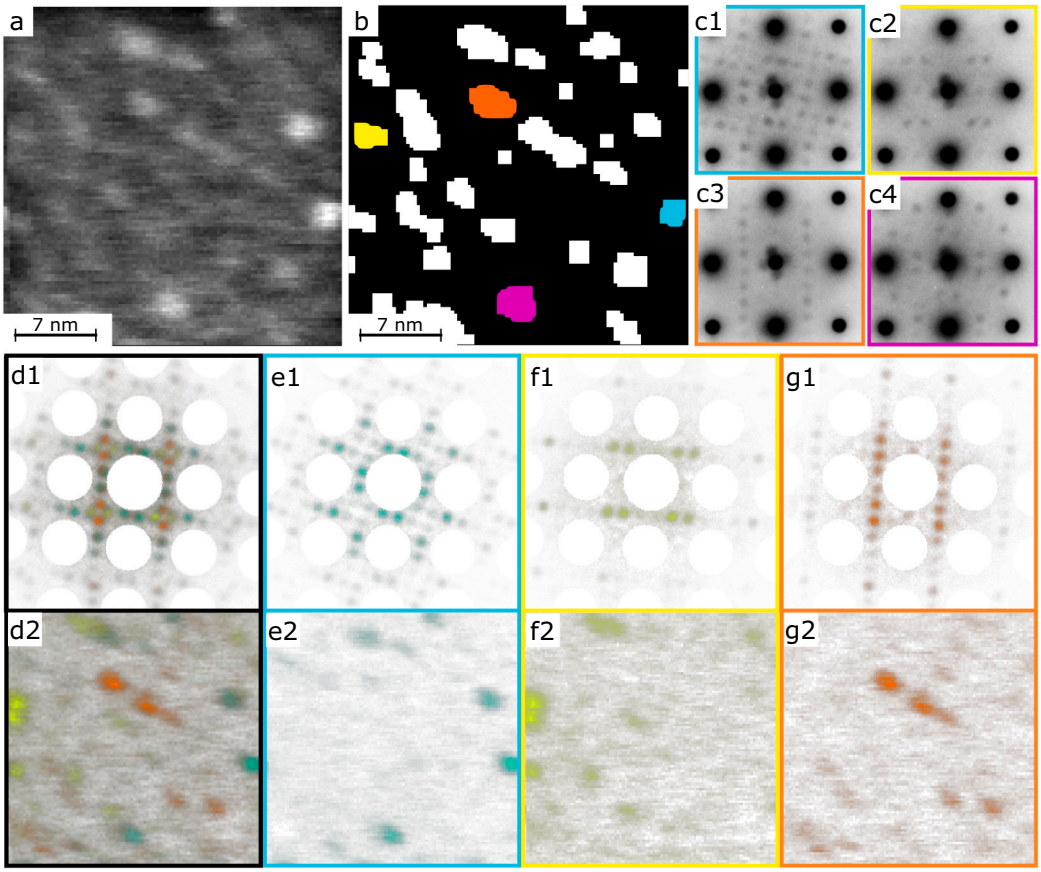

Fig. 6. One of the sped datasets investigated. a: VDF image. b: Binary VDF image. Colours indicate regions where the average PED patterns, seen in c1-c4, were extracted from. d1, d2: Composite component- and loading maps from all the NMF components associated with GPI zones. e1-g1: Component maps. e2-g2: Loading maps.

Out of 39 identifiable patterns, all the PED patterns viewed along [001]GPI were found to be ⟨411⟩ connected GPI zones except one, which was categorised as a ⟨330⟩-⟨411⟩ connected GPI zone. In one third (31%) of the GPI zones, [001]GPI was parallel to the viewing direction, the rest had [001]GPI normal to the viewing direction, c.f. column 4 and 5 in Fig. 5. This is reasonable, as [001]GPI has no preference for a specific ⟨001⟩Al direction. The diffracted intensity from a GPI zone was lowest in the direction normal to [001]GPI, making quantification harder. Although only 39 patterns were identifiable, the current HAADF-STEM experiments together with our previous work [9] support that the ⟨411⟩ connected GPI zones are more common than the ⟨330⟩-⟨411⟩ connected ones.

The simulated NBD patterns shown in Fig. 5 assume GPI zones of the same thickness as the Al along the ⟨001⟩ viewing direction. However, in reality the GPI zones are embedded in the Al matrix. This discrepancy between the models and reality hinders the extraction of quantitative information (such as GPI zone length/thickness) based on the intensities in the experimental patterns. Other factors also affect the intensity; these include the size of the GPI zones, their position inside the TEM sample, the thickness of the sample and the precession of the incoming beam. To investigate these effects, PED- and NBD patterns were simulated for two specimen thicknesses, as well as models having the GPI zone at the top or bottom surface. The results are shown in the Supplementary (Fig. 2). From the simulations, it is concluded that both specimen thickness and relative height of the GPI zone influence the intensity. Thus, only the position of the reflections, and not the relative intensities, should be used to identify the variant. Moreover, the precession affects the intensities of the unique reflections. It is observed that under certain circumstances, NBD yields a higher intensity in the reflections used for the profile plots in Supplementary Fig. 2, while under other circumstances, PED yields a higher intensity. Based on the simulations alone, one could conclude that it is ambiguous which operation mode is best fit for studying the GPI zones. However, the simulations are for a specific, ideal case. The experimental sample can incorporate artefacts from the sample preparation such as Cu-rich surface layers [41] or hydrocarbon contamination building up during TEM acquisition. Such layers affect the experimental diffraction patterns and are not accounted for in the simulations. The contamination can be lowered by decreasing the electron dose. However, in the case of studying GPI zones, a step size of 0.3 nm is needed to obtain sufficient resolution. In our experience, the precession improves the quality of the patterns by averaging out the signal from the contamination. The diffraction patterns also appear more even with precession, c.f. Supplementary Fig. 2.

3.4. Stability of the GPI zones

DFT calculations were performed to investigate the stability of the models in Fig. 5. The nomenclature is adapted from Ref. [9]: The models are denoted n-i$Z_6M_8Z_{24}$. The ‘n’ refers to either a pure ⟨411⟩ connected GPI zone or a ⟨330⟩-⟨411⟩ connected GPI zone, where we use '4' or '3′, respectively. A lowercase ‘i’ or ‘d’ refers to interstitial or defect in the central column of the TCO, respectively. For the fcc variant, the character is omitted. The last part describes the atoms of the three shells in the TCO: ‘Z6’ indicates there are six Zn atoms at the faces of the inner cube, ‘M8’ refers to the eight Mg atoms at the corner of the cube and ‘Z24’ gives the number of Zn atoms in the 24 atom shell immediately outside the cube.

The results from the DFT calculations are shown in Table 1. The pure

Table 1
GPI zones formation enthalpies and pressure in a 6×6×2 Al calculation cell, as ranked by formation enthalpy per solute. See the main text for explanation of the GPI zone configurations.

Configuration/composition			Formation enthalpy [eV]			Pressure	Ratio
No	GPI zone	Composition	Total	Atom	Solute	[kbar]	Zn/Mg
1	4-d$Z_6M_8Z_{24}$	$Mg_{32}Zn_{120}$	−22.078	−0.077	−0.145	1.9	3.750
2	3-d$Z_6M_8Z_{24}$	$Mg_{24}Zn_{90}$	−15.838	−0.055	−0.139	2.2	3.750
3	4-$Z_6M_8Z_{24}$[a]	$Mg_{32}Zn_{120}$	−20.037	−0.070	−0.132	−5.6	3.750
4	4-i$Z_6M_8Z_{24}$[a]	$Mg_{32}Zn_{124}$	−20.258	−0.069	−0.130	5.5	3.875
5	3-$Z_6M_8Z_{24}$	$Mg_{24}Zn_{90}$	−14.500	−0.050	−0.127	−3.8	3.750
6	3-i$Z_6M_8Z_{24}$	$Mg_{24}Zn_{93}$	−14.468	−0.050	−0.124	5.0	3.875

[a] Same model as previously published in Ref. [9]

⟨411⟩ connected GPI zones are consistently more energetically favourable than the ⟨330⟩-⟨411⟩ connected ones. We believe a reason for this is that ⟨330⟩ connected units have all Mg atoms on the same {001}Al planes, increasing strain for every new connection. It is seen that the defect variants have the lowest formation enthalpy per solute, followed by the fcc and interstitial variants, respectively.

Every TCO incorporating an occupied octahedral site will result in a vacancy in the Al matrix. The energy of the vacancy is its cohesive energy. Naturally, this energy penalty will be lowered if the vacancy disappears into a nearby defect, such as a particle or grain boundary. In the results of Table 1, the strictest energy penalty is given to the interstitial variants, where the vacancy is assumed to be absorbed by the matrix. This was not considered in our previous work [9], which found the interstitial variants to be the most energetically favourable.

For both the ⟨411⟩- and ⟨330⟩-⟨411⟩ connected GPI zones, the DFT calculations find that the defect variant is energetically more favourable than the fcc variant. The SPED data gave indications that these configurations could co-exist. Based on this, we propose a transition from the fcc variant to the defect variant as shown in Fig. 7, where the formation enthalpy is plotted against pressure. For simplicity, the TCOs are shown without the outer Zn rich shell in the figure. Initially, all the solutes should occupy fcc lattice positions. To alleviate the pressure, the atoms of the central columns move 2.025 Å in the ⟨001⟩Al direction along [001]GPI. This creates the 1D column defect which is also found in β'' [40] in the Al-Mg-Si alloy system, and the new configuration obtains a significantly lower enthalpy.

Although the interstitial configuration appears less energetically favourable than the fcc- and defect variants, the SPED data indicated that some of the GPI zones contained 3/2 occupied central columns. By inspection of the experimental diffraction pattern of the defect- and interstitial variant in column 5 in Fig. 5b-c, respectively, it can be seen that there is a common row of reflections. The PED pattern from the interstitial variant exhibits an extra row of reflections compared to the common one, as evidenced in the simulations in column 4 in Fig. 5b-c. We note that in the experimental pattern of the interstitial variant in column 5 in Fig. 5c, the extra row of reflections is weaker than the common one. This could indicate that the interstitial variant does not exist in a 'pure state', but rather exists in GPI zones where the central column in a TCO string is a mixture of both defects and interstitials along [001]GPI.

4. Conclusion

In this work, a TEM-based methodology for studying GP zones with periodic structure embedded in the Al matrix has been developed. Data was collected from an Al-Zn-Mg alloy containing a dense population of GPI zones. Electron diffraction patterns from single GPI zones were successfully recorded by a direct electron detector with the TEM operated in the SPED mode. The GPI zones are spherical particles with a diameter of 1 to 3 nm embedded in the host Al matrix. The experimental diffraction patterns were compared with multi-slice simulations based on the previously proposed structures of the GPI zones. A good correspondence was found between the two. The technique allows 3D information to be obtained, since the resolution in reciprocal space is sufficient to extract information in ⟨001⟩Al zones, from individual GPI zones viewed both along their unique axis, [001]GPI, and the normal orientations, which is not possible from HAADF-STEM imaging alone. By taking advantage of this, it was found that the central column of the

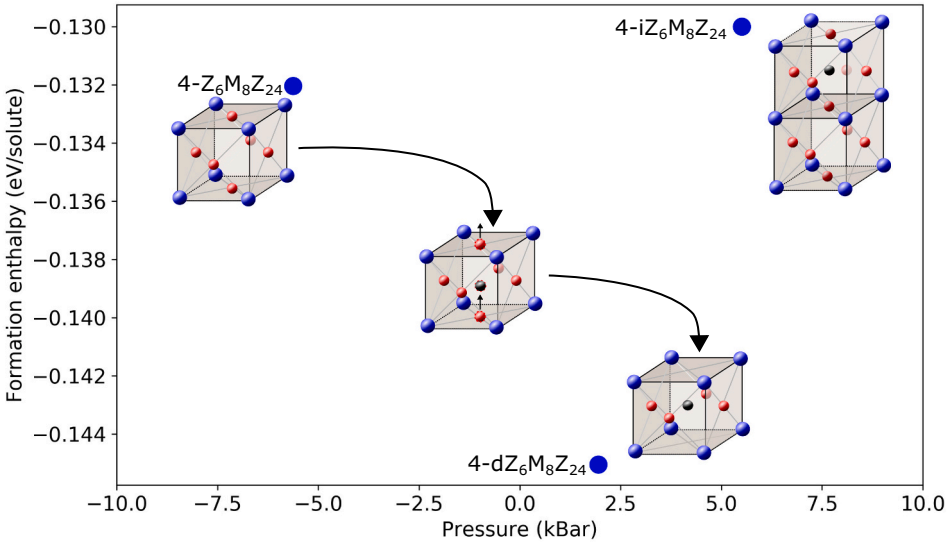

Fig. 7. Formation enthalpy given in eV/solute vs. pressure for the ⟨411⟩ connected GPI zones. In the schematics of the TCOs, the outer Zn rich layer is omitted for simplicity. (1) fcc variant, (2) defect variant and (3) shows the interstitial variant.

molecular building block of the GPI zones may be shifted one atomic plane compared to the Al fcc positions. This was supported by DFT calculations. The presented methodology is believed to be highly useful also for other material systems where small particles are embedded in a host material.

Author contribution

E.T., C.D., S.W. and R.H. conceived, designed and supervised the research. E.T. conducted the (S)TEM experiments. S.J.A. created the initial models. J.Fra. and J.Fri. prepared the models and conducted the DFT modelling. E.T. conducted the diffraction simulations. E.T. prepared the figures. E.T. wrote the manuscript with input from all the authors.

Data availability

The raw data and models used to reproduce the presented results are available in the Zenodo repository https://doi.org/10.5281/zenodo.5092880.

Declaration of Competing Interest

The authors declare that they have no known competing financial interests or personal relationships that could have appeared to influence the work reported in this paper.

Acknowledgements

This work was supported by the NTNU Digital Transformation initiative'Alldesign' (E.T., J.Fri. and R.H.) and The Research Council of Norway (NFR) through the project'SumAl' (NFR: 294933) (J.Fri., J.Fra., C.D.M., R.H. & S.J.A.), supported by Hydro, Benteler Automotive Raufoss AS and Neuman Aluminium. The (S)TEM work was conducted on the NORTEM (NFR: 197405) infrastructure at the TEM Gemini Centre, Trondheim, Norway. The DFT calculations were performed on resources provided by UNINETT Sigma2 - the National Infrastructure for High Performance Computing and Data Storage in Norway (NN8068K). We acknowledge A. Bendo and K. Matsuda at the University of Toyama for providing the alloy studied in this work. We acknowledge E. Christiansen and J. K. Sunde who wrote the initial code for analyzing the SPED data which has been further developed in this work.

Appendix A. Supplementary data

Supplementary data to this article can be found online at https://doi.org/10.1016/j.matchar.2021.111675.

References

[1] P. Hartel, H. Rose, C. Dinges, Conditions and reasons for incoherent imaging in STEM, Ultramicroscopy 63 (1996) 93–114, https://doi.org/10.1016/0304-3991(96)00020-4.
[2] S.J. Andersen, C.D. Marioara, J. Friis, S. Wenner, R. Holmestad, Precipitates in aluminium alloys, Adv. Phys. X 3 (2018) 1479984, https://doi.org/10.1080/23746149.2018.1479984.
[3] T. Saito, E.A. Mørtsell, S. Wenner, C.D. Marioara, S.J. Andersen, J. Friis, K. Matsuda, R. Holmestad, Atomic structures of precipitates in Al-Mg-Si alloys with small additions of other elements, Adv. Eng. Mater. 20 (2018) 1800125, https://doi.org/10.1002/adem.201800125.
[4] A. Wilm, Physikalisch-metallurgische Untersuchungen über magnesiumhaltige Aluminiumlegierungen, Metallurgie 8 (1911) 225–227.
[5] E. Hornbogen, Hundred years of precipitation hardening, J. Light. Met. 1 (2001) 127–132, https://doi.org/10.1016/S1471-5317(01)00006-2.
[6] A. Guinier, Structure of Age-Hardened Aluminium-Copper Alloys, 1938. URL, https://www.nature.com/articles/142569b0, https://doi.org/10.1038/142569b0.
[7] G. Preston, The diffraction of X-rays by an age-hardening alloy of aluminium and copper. The structure of an intermediate phase, Lond. Edinburgh Dublin Philos. Mag. J. Sci. 26 (1938) 855–871, https://doi.org/10.1080/14786443808562177.
[8] L.K. Berg, J. Gjøønnes, V. Hansen, X.Z. Li, M. Knutson-Wedel, G. Waterloo, D. Schryvers, L.R. Wallenberg, GP-zones in Al-Zn-Mg alloys and their role in artificial aging, Acta Mater. 49 (2001) 3443–3451, https://doi.org/10.1016/S1359-6454(01)00251-8.
[9] A. Lervik, E. Thronsen, J. Friis, C.D. Marioara, S. Wenner, A. Bendo, K. Matsuda, R. Holmestad, S.J. Andersen, Atomic structure of solute clusters in Al–Zn–mg alloys, Acta Mater. 205 (2021), 116574, https://doi.org/10.1016/j.actamat.2020.116574.
[10] H. Löffler, I. Kovács, J. Lendvai, Decomposition Processes in Al-Zn-Mg Alloys, 1983, https://doi.org/10.1007/BF00541825.
[11] G. Dlubek, R. Krause, O. Brümmer, F. Plazaola, Study of formation and reversion of Guinier-Preston zones in Al-4.5 at%Zn-x at%Mg alloys by positrons, J. Mater. Sci. 21 (1986) 853–858, https://doi.org/10.1007/BF01117364.
[12] V. Hansen, O.B. Karlsen, Y. Langsrud, J. Gjønnes, Precipitates, zones and transitions during aging of Al - Zn - Mg - Zr 7000 series alloy, Mater. Sci. Technol. 20 (2004) 185–193, https://doi.org/10.1179/026708304225010424.
[13] J. Buha, R.N. Lumley, A.G. Crosky, Secondary ageing in an aluminium alloy 7050, Mater. Sci. Eng. A 492 (2008) 1–10, https://doi.org/10.1016/j.msea.2008.02.039.
[14] M. Torsæter, H.S. Hasting, W. Lefebvre, C.D. Marioara, J.C. Walmsley, S. J. Andersen, R. Holmestad, The influence of composition and natural aging on clustering during preaging in Al-Mg-Si alloys, J. Appl. Phys. 108 (2010) 073527, https://doi.org/10.1063/1.3481090.
[15] Y. Aruga, M. Kozuka, Y. Takaki, T. Sato, Evaluation of solute clusters associated with bake-hardening response in isothermal aged Al-Mg-Si alloys using a three-dimensional atom probe, Metallurg. Mater. Trans. A: Phys. Metallurg. Mater. Sci. 45 (2014) 5906–5913, https://doi.org/10.1007/s11661-014-2548-y.
[16] H. Zhao, B. Gault, D. Ponge, D. Raabe, F. De Geuser, Parameter free quantitative analysis of atom probe data by correlation functions: application to the precipitation in Al-Zn-Mg-Cu, Scr. Mater. 154 (2018) 106–110, https://doi.org/10.1016/j.scriptamat.2018.05.024.
[17] G. Sha, A. Cerezo, Early-stage precipitation in Al-Zn-Mg-Cu alloy (7050), Acta Mater. 52 (2004) 4503–4516, https://doi.org/10.1016/j.actamat.2004.06.025.
[18] G. McMullan, A.R. Faruqi, R. Henderson, N. Guerrini, R. Turchetta, A. Jacobs, G. van Hoften, Experimental observation of the improvement in MTF from backthinning a CMOS direct electron detector, Ultramicroscopy 109 (2009) 1144–1147, https://doi.org/10.1016/j.ultramic.2009.05.005.
[19] C. Ophus, Four-Dimensional Scanning Transmission Electron Microscopy (4D-STEM): From Scanning Nanodiffraction to Ptychography and Beyond, 2019, https://doi.org/10.1017/S1431927619000497.
[20] P.A. Midgley, A.S. Eggeman, Precession Electron Diffraction - A Topical Review, 2015, https://doi.org/10.1107/S2052252514022283.
[21] R. Vincent, P.A. Midgley, Double conical beam-rocking system for measurement of integrated electron diffraction intensities, Ultramicroscopy 53 (1994) 271–282, https://doi.org/10.1016/0304-3991(94)90039-6.
[22] J.K. Sunde, S. Wenner Paulsen, R. Holmestad, Precipitate statistics in an Al-Mg-Si-Cu alloy from scanning precession electron diffraction data, in: Journal of Physics: Conference Series vol. 902, Institute of Physics Publishing, 2017, p. 12022, https://doi.org/10.1088/1742-6596/902/1/012022.
[23] J.K. Sunde, C.D. Marioara, A.T.J. van Helvoort, R. Holmestad, The evolution of precipitate crystal structures in an Al-Mg-Si(-Cu) alloy studied by a combined HAADF-STEM and SPED approach, Mater. Charact. 142 (2018) 458–469, https://doi.org/10.1016/j.matchar.2018.05.031.
[24] J.K. Sunde, C.D. Marioara, R. Holmestad, The effect of low Cu additions on precipitate crystal structures in overaged Al-Mg-Si(-Cu) alloys, Mater. Charact. 160 (2020), 110087, https://doi.org/10.1016/j.matchar.2019.110087.
[25] J.K. Sunde, D.N. Johnstone, S. Wenner, A.T. van Helvoort, P.A. Midgley, R. Holmestad, Crystallographic relationships of T-/S-phase aggregates in an Al–Cu–Mg–Ag alloy, Acta Mater. 166 (2019) 587–596, https://doi.org/10.1016/j.actamat.2018.12.036.
[26] J.S. Barnard, D.N. Johnstone, P.A. Midgley, High-resolution scanning precession electron diffraction: alignment and spatial resolution, Ultramicroscopy 174 (2017) 79–88, https://doi.org/10.1016/j.ultramic.2016.12.018.
[27] J.A. Mir, R. Clough, R. MacInnes, C. Gough, R. Plackett, I. Shipsey, H. Sawada, I. MacLaren, R. Ballabriga, D. Maneuski, V. O'Shea, D. McGrouther, A.I. Kirkland, Characterisation of the Medipix3 detector for 60 and 80 keV electrons, Ultramicroscopy 182 (2017) 44–53, https://doi.org/10.1016/j.ultramic.2017.06.010.
[28] F.D.L. Peña, E. Prestat, V.T. Fauske, P. Burdet, T. Furnival, P. Jokubauskas, M. Nord, T. Ostasevicius, J. Lähnemann, K.E. MacArthur, D.N. Johnstone, M. Sarahan, J. Taillon, T. Aarholt, Pquinn-Dls, V. Migunov, A. Eljarrat, J. Caron, T. Poon, S. Mazzucco, B. Martineau, S. Somnath, T. Slater, C. Francis, M. Walls Actions-User, N. Tappy, N. Cautaerts, F. Winkler, G. Donval, hyperspy/hyperspy: Release v1.6.3, 2021, https://doi.org/10.5281/ZENODO.4923970.
[29] D.N. Johnstone, P. Crout, M. Nord, J. Laulainen, S. Høgås, B. Martineau EirikOpheim, C. Francis, T. Bergh, E. Prestat, S. Smeets, S. Collins Andrew-rossl, I. Hjorth, T. Furnival Mohsen, D. Jannis, N. Cautaerts, E. Jacobsen, T. Poon AndrewHerzing, H.W. Anes, J. Morzy, S. Huang, T. Doherty Phillipcrout, T. Ostasevicius Affaniqbal, R. Tovey Mvonlany, pyxem/pyxem: pyxem 0.13.1, 2021. URL.
[30] S. van der Walt, J.L. Schönberger, J. Nunez-Iglesias, F. Boulogne, J.D. Warner, N. Yager, E. Gouillart, T. Yu, The scikit-image contributors, scikit-image: image processing in Python, PeerJ 2 (2014), e453, https://doi.org/10.7717/peerj.453.
[31] S.R. Sternberg, Biomedical image processing, Computer 16 (1983) 22–34, https://doi.org/10.1109/MC.1983.1654163.
[32] A.C. Bovik, The Essential Guide to Image Processing, Elsevier Inc., 2009, https://doi.org/10.1016/B978-0-12-374457-9.X0001-7.
[33] D.D. Lee, H.S. Seung, Learning the parts of objects by non-negative matrix factorization, Nature 401 (1999) 788–791. URL.

[34] B.H. Martineau, D.N. Johnstone, A.T. van Helvoort, P.A. Midgley, A.S. Eggeman, Unsupervised machine learning applied to scanning precession electron diffraction data, Adv. Struct. Chem. Imaging 5 (2019) 1–14, https://doi.org/10.1186/s40679-019-0063-3.
[35] G. Kresse, J. Hafner, Ab initio molecular dynamics for liquid metals, Phys. Rev. B 47 (1993) 558–561, https://doi.org/10.1103/PhysRevB.47.558.
[36] G. Kresse, J. Furthmüller, Efficient iterative schemes for ab initio total-energy calculations using a plane-wave basis set, Phys. Rev. B - Condens. Matter Mater. Phys. 54 (1996) 11169–11186, https://doi.org/10.1103/PhysRevB.54.11169.
[37] P.E. Blöchl, Projector augmented-wave method, Phys. Rev. B 50 (1994) 17953–17979, https://doi.org/10.1103/PhysRevB.50.17953.
[38] G. Kresse, D. Joubert, From ultrasoft pseudopotentials to the projector augmented-wave method, Phys. Rev. B - Condens. Matter Mater. Phys. 59 (1999) 1758–1775, https://doi.org/10.1103/PhysRevB.59.1758.
[39] L.J. Allen, A.J. D'Alfonso, S.D. Findlay, Modelling the inelastic scattering of fast electrons, Ultramicroscopy 151 (2015) 11–22, https://doi.org/10.1016/j.ultramic.2014.10.011.
[40] M.A. Van Huis, M.H. Sluiter, J.H. Chen, H.W. Zandbergen, Concurrent substitutional and displacive phase transformations in Al-Mg-Si nanoclusters, Phys. Rev. B - Condens. Matter Mater. Phys. 76 (2007) 174113, https://doi.org/10.1103/PhysRevB.76.174113.
[41] S. Wenner, A. Lervik, E. Thronsen, C.D. Marioara, S. Kubowicz, R. Holmestad, Copper enrichment on aluminium surfaces after electropolishing and its effect on electron imaging and diffraction, Mater. Charact. 172 (2021), 110846, https://doi.org/10.1016/j.matchar.2020. 110846.